Molecular model for chirality phenomena

Folarin Latinwo,[1] Frank H. Stillinger,[2,a)] and Pablo G. Debenedetti[1,b)]
[1]*Department of Chemical and Biological Engineering, Princeton University, Princeton, New Jersey 08544, USA*
[2]*Department of Chemistry, Princeton University, Princeton, New Jersey 08544, USA*

(Received 15 July 2016; accepted 28 September 2016; published online 17 October 2016)

Chirality is a hallmark feature for molecular recognition in biology and chemical physics. We present a three-dimensional continuum model for studying chirality phenomena in condensed phases using molecular simulations. Our model system is based upon a simple four-site molecule and incorporates non-trivial kinetic behavior, including the ability to switch chirality or racemize, as well as thermodynamics arising from an energetic preference for specific chiral interactions. In particular, we introduce a chiral renormalization parameter that can locally favor either homochiral or heterochiral configurations. Using this model, we explore a range of chirality-specific phenomena, including the kinetics of chiral inversion, the mechanism of spontaneous chiral symmetry breaking in the liquid, chirally driven liquid-liquid phase separation, and chiral crystal structures. *Published by AIP Publishing.* [http://dx.doi.org/10.1063/1.4964678]

I. INTRODUCTION

The building blocks of life are inherently chiral. Amino acids, as found in proteins, and monosaccharides, as found in RNA or DNA, possess forms that are each nonsuperimposable with their respective mirror images. In general, equilibrium template-free laboratory synthesis of a given chiral compound will yield a racemic mixture, i.e., an equal proportion of its two chiral forms identified typically as L- or D- enantiomers. However, *all* naturally occurring chiral proteinogenic amino acids exist exclusively as L-enantiomers, as identified by the chirality of their α-carbon, while most naturally occurring monosaccharides exist as D-enantiomers, as identified by the chirality of the carbon furthest removed from the carbonyl group. These observations lead to fundamental questions regarding the origin of biological homochirality, especially in light of the fact that chirality is essential for life as we know it.[1,2]

From a practical perspective, molecular handedness or chirality in biology places stringent requirements on pharmaceutical processing.[3,4] Different enantiomers of a given molecule can have very dissimilar physiological effects. Specific examples include the tuberculosis drug ethambutol, which possesses an enantiomer that lacks antimicrobial activity, and the morning sickness as well as cancer drug thalidomide, which possesses an enantiomer known to cause birth defects. Accordingly, the pharmaceutical industry pursues the development of design principles for asymmetric synthesis[5,6] or efficient separation[7] of chirality-tailored compounds.

In addition to the above examples in pharmacology, chirality plays a key role in advanced photonics applications,[8,9] in low-power electronic display technologies,[10,11] and in the processing of amorphous pharmaceuticals.[12] A specific example relevant to processing concerns the area of pressure-induced crystallization. Whereas high pressures increase the rate of crystallization of supercooled achiral and enantiopure liquids,[13] recent experiments have shown the opposite effect for racemic mixtures of analgesic drugs such as ketoprofen and ibuprofen.[14,15] In light of such interesting findings, molecular level insight is crucial to guide the development of processing techniques for chiral compounds.

Industrial processing has not been the sole focus of chirality-related research. Understanding the emergence of biological homochirality in nature has also been the focus of much research activity. The following two broad questions summarize the field: Was our homochiral fate predetermined or stochastic? What are plausible scenarios that can explain the emergence and persistence of chiral symmetry breaking? These questions have puzzled scientists for over a century and remain a subject of debate.

In the predetermined scenario, broken chiral symmetry associated with the weak interaction or the presence of an excess of right-circularly polarized light in interstellar molecular clouds (which causes enantioselective photolysis of D-amino acid enantiomers[16]) is often cited as causes of our present biological homochirality.[17–19] In contrast, the stochastic scenario posits that the effect of the weak force is miniscule,[20] and that a realization of life with D-amino acids and L-sugars is equally likely as its reverse (L-amino acids and D-sugars) in life as we know it. Nevertheless, in both scenarios, any small initial local chiral bias is generally considered insufficient for the widespread emergence of uniform biological homochirality. As a consequence, a mechanism for chiral amplification and preservation is required for the macroscopic emergence of homochirality.[19]

Chiral amplification schemes are broadly classified into physical and chemical mechanisms. A prominent chemical mechanism (the Frank model) involves a reaction scheme with autocatalysis and chiral inhibition that is sufficient to yield a homochiral state.[21] Despite the theoretical validity

a)fhs@princeton.edu
b)pdebene@princeton.edu

of this scheme, an experimental demonstration remained elusive until the discovery of the Soai reaction.[22,23] From a theoretical perspective, kinetic models[24] and lattice-based calculations[25,26] have provided mechanistic and microscopic insights into the Frank model. A recent theoretical modification of the Frank model suggests that chiral inhibition is not necessary to achieve biological homochirality.[27] Interestingly, that work predicts that multiplicative stochasticity, in which the strength of fluctuations in a system is dependent on its instantaneous configuration,[28,29] in conjunction with autocatalysis is sufficient to break chiral symmetry.

In the context of polymerization reactions, statistical considerations and experimental evidence suggest that homochirality is a direct consequence of an efficient assembly of chiral monomeric units.[30–33] However, the discovery of chiral cross-inhibition, i.e., a racemic pool of reactants inhibits the rate of templated-homochiral polymerization,[34] suggests that chiral symmetry breaking likely occurred in a prebiotic world, assuming that life is necessarily chiral. As a consequence, intense research effort has focused on the development of alternative polymerization[35,36] and non-polymerization[22] mechanisms that break chiral symmetry. More recently, an alternative polymerization scenario that relies on racemic prebiotic conditions for chiral symmetry breaking has been demonstrated.[37]

For physical mechanisms, chiral amplification is realizable under both equilibrium and far-from-equilibrium conditions. Notable examples include systems that display chirality-dependent solid-liquid phase equilibria combined with accessible racemization kinetics or "chiral amnesia," i.e., the molecules have the ability to lose chiral identity in solution.[38,39] In these systems, the difference in the relative stability of conglomerate (enantiopure) and racemic crystals provides a driving force for chiral symmetry breaking.[40–44] Although a two-dimensional lattice model has provided rich molecular-level insight into the specific interactions required for such phenomena,[45] a three-dimensional continuum molecular model for general chirality phenomena has remained desirable but elusive.

In this work, we present a simple three-dimensional continuum molecular model system for chirality phenomena. Inspired by the smallest chiral molecule in nature, hydrogen peroxide,[46–48] we developed a tetramer model that exhibits tunable chiral interactions, chiral amnesia, as well as solid-phase chiral behavior, all of which are relevant features for chiral symmetry breaking. In Sec. II, we provide details of the molecular model including the nature of its interactions with achiral solvents. In Sec. III, we present results for calculations on chiral inversion kinetics, chiral liquid immiscibility, and a candidate enantiopure crystal structure. In Sec. IV, we provide concluding remarks and suggest some possible directions for future inquiry.

II. MODEL AND METHODS

A. Intramolecular potential and chirality measure for isolated chiral tetramer

Geometrically, the instantaneous state of the chiral tetramer is completely specified by the location of "nuclei" or "monomers" along a three-bond backbone at $\mathbf{r}_1, \mathbf{r}_2, \mathbf{r}_3, \mathbf{r}_4$, respectively, as shown in Fig. 1. Each of these four units is assigned a common mass m. Based on the geometry of the tetramer molecule, the intramolecular potential energy function $\Phi^{(1)}$ includes contributions from (two-site) bond stretching, (three-site) bond angle deformations, and (four-site) rotations about the dihedral angle such that

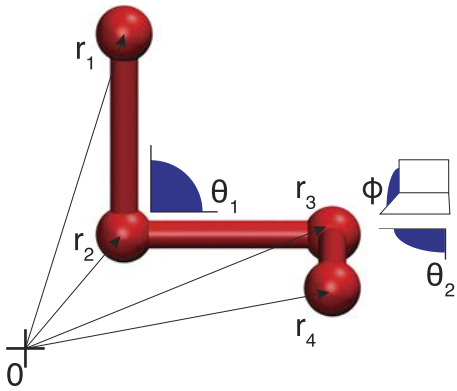

FIG. 1. Molecular configuration and relevant geometrical features of the chiral tetramer. The features include the position vectors $\mathbf{r}_i$ of tetramer monomers, the bond angles θ_i, and the dihedral angle ϕ of the tetramer.

$$\Phi^{(1)}(\{\mathbf{r}_i\}) = \sum_{i=1}^{3} \frac{k_s}{2}(r_{i,i+1} - b)^2 + \sum_{i=1}^{2} \frac{k_b}{2}\left(\theta_i - \frac{\pi}{2}\right)^2 + k_d \cos^2\phi. \tag{1}$$

Here b represents the equilibrium bond length, the θ_i represent the bond angles in radians, ϕ is the dihedral angle in radians, and k_s, k_b, k_d represent the force constants for bond stretching, angle bending, and dihedral motions, respectively. We obviously require that $b, k_s, k_b, k_d > 0$. Note that our choice of quadratic dependence on the cosine of the dihedral angle ensures that our tetramers possess only two energetically equivalent but geometrically distinct states at mechanical equilibrium. Figure 2 shows the intramolecular potential energy of an otherwise undeformed isolated tetramer as a function of its dihedral angle. The tetramer is at mechanical equilibrium at the dihedral angles $\phi = \pm\pi/2$.

In order to monitor the chirality of the tetramers, and to control the homochiral *vs.* heterochiral bias of intermolecular interactions, we introduce a scalar chirality measure, $-1 \le \zeta \le +1$, for each tetramer,

$$\zeta(\mathbf{r}_1, \mathbf{r}_2, \mathbf{r}_3, \mathbf{r}_4) = \frac{\mathbf{r}_{12} \cdot (\mathbf{r}_{23} \times \mathbf{r}_{34})}{|\mathbf{r}_{12}|\,|\mathbf{r}_{23}|\,|\mathbf{r}_{34}|}. \tag{2}$$

This quantity attains its upper and lower limits for the pair of mechanically stable, mirror image, $\Phi^{(1)}$ minima, and it vanishes for the "*cis*" and "*trans*" planar transition states that are illustrated at the top of Fig. 2. The general form of ζ is consistent with other scalar measures of chirality routinely employed in liquid crystalline systems.[49,50] So far as overall chirality classification is concerned, a binary distinction depending on the numerical sign of ζ suffices. This immediately allows evaluation of the traditional "enantiomeric excess" for any given collection of tetramers. It should be noted in passing that normal mode analysis for an isolated tetramer in either the "*cis*" or "*trans*" transition state reveals

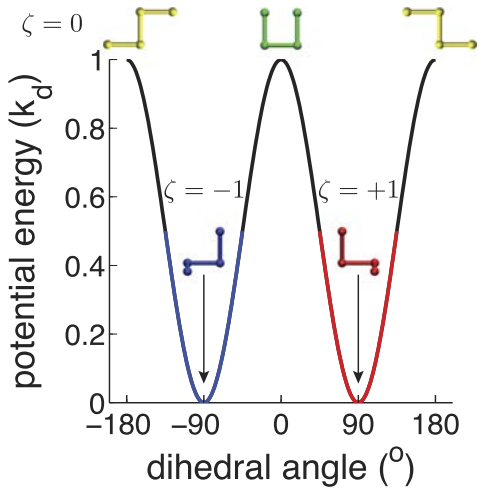

FIG. 2. Intramolecular potential energy of an isolated tetramer as a function of molecule dihedral angle. Enantiomers of the tetramer (at mechanical equilibrium) are shown in red and blue, respectively. The *cis* and *trans*-transition states are shown in green and yellow respectively. The chirality measure (defined in text), ζ, distinguishes between enantiomers and achiral transition states. Note that the *trans*-configurations shown in yellow are identical and should not be confused as being chiral.

five positive, six vanishing, and one imaginary harmonic normal mode frequencies, the last of which is identical for the *cis* and *trans*-cases and is directed along the ideal reaction pathway.

In contrast to the four-site chirality geometry of the present model, the frequently encountered case of a carbon stereocenter chemically bonded to four surrounding distinguishable ligands does not appear to possess a correspondingly simple and direct chirality measure. In particular, it is unclear that what such five-center molecules would require for a configurational analog to the enantiomer dividing hypersurface $\zeta = 0$, and whether all of its transition states would lie precisely on that hypersurface.

B. Chirality renormalization and intermolecular interactions

In specifying the intermolecular interactions, we consider a pair potential energy function of chiral character. The intermolecular interactions utilize information encoded by the chirality of the molecules as presented in Eq. (2). In particular, the intermolecular potential energy function $\Phi^{(2)}$ between two molecules identified by α and γ is given as a sum of 16 terms for each pair of monomers, one from each of the two tetramers,

$$\Phi^{(2)}\left(\{\mathbf{r}_i^\alpha\},\{\mathbf{r}_j^\gamma\}\right) = \sum_{i,j=1}^{4} \epsilon_{tt}(\zeta^\alpha,\zeta^\gamma)\, v\left(\frac{\left|\mathbf{r}_i^\alpha - \mathbf{r}_j^\gamma\right|}{\sigma_{tt}}\right). \quad (3)$$

Here σ_{tt} is the pair potential length parameter which specifies the range of the intermolecular interactions, and the general function $\epsilon v\,(r/\sigma)$ is chosen to be the 12-6 Lennard-Jones (L-J) pair potential. The strength of the interaction energy ϵ_{tt} is a function of the chirality measures $\zeta^\alpha, \zeta^\gamma$ for a given pair of tetramers, so as to favor or to disfavor the interactions between homochiral and heterochiral entities, i.e., the same or opposite enantiomers. In particular, the form of the interaction strength is chosen to be

$$\epsilon_{tt}(\zeta^\alpha,\zeta^\gamma) = \epsilon_0\left[1 + \lambda\zeta\left(\mathbf{r}^\alpha_{i=1,2,3,4}\right)\zeta\left(\mathbf{r}^\gamma_{i=1,2,3,4}\right)\right], \quad (4)$$

where λ is the chirality renormalization parameter, subject to $|\lambda| < 1$. This parameter represents a measure of the *chiral bias* such that at low to moderate pressure, $\lambda < 0$ locally favors racemic or heterochiral interactions (i.e., when $\mathrm{sgn}(\zeta^\alpha\zeta^\gamma)$ is negative), $\lambda > 0$ locally favors homochiral or enantiopure interactions (i.e., when $\mathrm{sgn}(\zeta^\alpha\zeta^\gamma)$ is positive), and $\lambda = 0$ represents a bias-free scenario. Equation (4) is a key feature of the model.

We stress that the chiral renormalization parameter represents a coarse-graining route that accounts for the local preferences of a pair of chiral entities to be in proximity at low temperatures. Real substances display these local binding preferences. For instance, aspartic acid, tartaric acid, and glutamic acid each displays a local homochiral bias ($\lambda > 0$) evident from their conglomerate (i.e., enantiopure) crystal structures, while serine and histidine each displays local heterochiral bias ($\lambda < 0$) evident from their racemic (alternating enantiomers) crystal structures. Of course, the numerical value for the chiral renormalization parameter is system-specific and will depend on the details of hydrogen bonding, electrostatic, and dispersive interactions. Consequently, the underlying intention of our tetramer model is to image as many different chiral substances as possible, whether they involve underlying detailed enantiopure or racemic interactions.

C. Achiral solvents

For the purpose of analyzing the solvation behavior of the tetramer model, we specify solvent-solvent (ss) and solvent-tetramer (st) interparticle interactions. We will consider N_s structureless and spherically symmetric particles located at positions $\mathbf{s}^\delta$, $1 \le \delta \le N_s$. For simplicity, we will use the same generic isotropic pair potential function v utilized in Eq. (3) to define the solvent-based interactions but without chirality renormalization. The specification of these interactions requires energy and distance parameters designated by ϵ_{ss}, σ_{ss} and ϵ_{st}, σ_{st}, respectively. Based on these choices, the total potential energy function, Φ, of a system consisting of N_t tetramers and N_s solvent particles is given as

$$\begin{aligned}\Phi\left(\{N_t\},\{N_s\}\right) = &\sum_{\alpha=1}^{N_t}\Phi^{(1)}\left(\mathbf{r}^\alpha_{i=1,2,3,4}\right)\\ &+\sum_{\alpha=1}^{N_t-1}\sum_{\gamma=\alpha+1}^{N_t}\Phi^{(2)}\left(\mathbf{r}^\alpha_{i=1,2,3,4},\mathbf{r}^\gamma_{j=1,2,3,4}\right)\\ &+\sum_{\delta=1}^{N_s-1}\sum_{\mu=\delta+1}^{N_s}\epsilon_{ss}v\left(\frac{\left|\mathbf{s}^\delta-\mathbf{s}^\mu\right|}{\sigma_{ss}}\right)\\ &+\sum_{\alpha=1}^{N_t}\sum_{\delta=1}^{N_s}\sum_{i=1}^{4}\epsilon_{st}v\left(\frac{\left|\mathbf{r}_i^\alpha-\mathbf{s}^\delta\right|}{\sigma_{st}}\right). \quad (5)\end{aligned}$$

Equation (5) completely specifies the potential energy function required for analyzing the solvation behavior of our tetramer

TABLE I. Parameters for chiral tetramers.

Units	k_s (kcal/mol Å^2)	k_b (kcal/mol rad^2)	k_d (kcal/mol)	b Å	m (g/mol)	ϵ_0 (kcal/mol)	σ_{tt} Å
Real	1000	100.0	2.775	1.18	8.5	0.15 535	1.115
Reduced	8003	643.7	17.86	1.0583	1	1	1

model. We stress that in contrast with the interaction energy (ϵ_{tt}) between two tetramers, the interaction energy (ϵ_{st}) between the solvent and the individual monomers in a tetramer does not possess any chiral character. It is, however, possible to allow for direct chirality-mediated solvent interactions by specifying the energetic solvent-tetramer interactions similar to Eq. (4). This consideration is beyond the scope of the current investigation. To maximize simplicity of our current model, we assign a common mass, m, to all of the force centers in the tetramer as well as to all of the solvent particles. In addition, we require common energy and length parameters for all Lennard-Jones interactions such that

$$\begin{aligned} \epsilon_0 &= \epsilon_{ss} = \epsilon_{st}, \\ \sigma_{tt} &= \sigma_{st} = \sigma_{ss}. \end{aligned} \tag{6}$$

Equations (1)-(6) completely specify the tetramer model and all of the interactions of a classical nature. In specifying physical values for the potential energy parameters, we have been guided by the molecular properties of hydrogen peroxide;[51–53] however, the reader should keep in mind that this model is not intended to be an accurate representation of that specific substance. The corresponding values chosen for our model are presented in Table I.

D. Reduced units

Given the elementary choice of parameters for mass m, energy ϵ_0, and distance σ_{tt}, we study our model as usual with reduced units. These units are chosen as $t^* = \sigma_{tt}\sqrt{m/\epsilon_0}$ = 0.4033 ps for the reduced time, $\rho^* = \sigma_{tt}^{-3}$ = 0.7214 Å^{-3} for the reduced density, $p^* = \epsilon_0\sigma_{tt}^{-3}$ = 7786 bar for the reduced pressure, and $T^* = \epsilon_0/k_B$ = 78.15 K for the reduced temperature, where k_B is the Boltzmann constant. Table I displays the interaction parameters both in real physical units and in reduced form.

E. Simulation procedure

To investigate the condensed phase behavior of our model, we implemented our calculations in the molecular dynamics (MD) package LAMMPS.[54] MD simulations were performed in both the canonical and isothermal-isobaric ensembles. The temperature and pressure were controlled using Nosé-Hoover thermostats and barostats, respectively. Periodic boundary conditions and a spherical cutoff ($2.5\sigma_{tt}$) minimum image convention for pair interactions were applied in all three directions. A time step of $0.0005t^*$ was used for the velocity-Verlet integrator, where t^* is the reduced time unit.

In addition to MD simulations, we also performed inherent structure calculations to provide further insight into our model. The inherent structures correspond to system configurations at local potential energy minima.[55,56] To determine the inherent structure energies, we performed local energy minimization of the system configuration using the conjugate-gradient method in LAMMPS with a potential energy convergence criterion of 1 part in 10 000. This choice proved sufficient in yielding an accurate estimate of inherent structures.

III. RESULTS AND DISCUSSION

A. Chiral racemization kinetics

First, we considered the racemization behavior of a single chiral tetramer in an achiral solvent. To this end, we studied the chiral inversion of an isolated tetramer molecule solvated in a Lennard-Jones fluid as described above. Here, our system comprises of one tetramer molecule and 4092 solvent molecules. Figure 3 shows the time evolution of the dihedral angle of the tetramer at two distinct temperatures. We observe that the chirality of the molecule, as measured by the dihedral angle, racemizes between its two stable enantiomorphs. The stochastic nature of the racemization is due to many-body interactions between the tetramer and the solvent molecules. A strong temperature dependence in the racemization rate is apparent. As expected, at the lower temperature (T = 2.0), the molecule persists longer in the vicinity of each stable enantiomorph relative to the higher temperature (T = 4.0). The temperature dependence of the racemization is further illustrated by the free energy profiles in Fig. 3. As expected, the free energy barrier to chirality inversion of a solvated tetramer increases as the temperature is lowered.

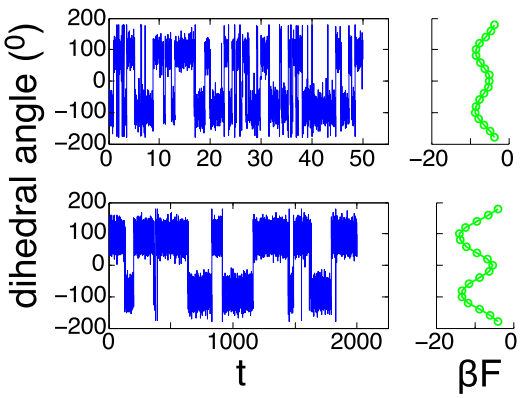

FIG. 3. Racemization kinetics and free energy profile of a single tetramer in a Lennard-Jones fluid at reduced density 0.66. The top and bottom panels correspond to results from canonical ensemble calculations at T = 4.0 and 2.0, respectively. The free energy F is determined as $\beta F = -\ln P$, where $\beta = \frac{1}{k_B T}$ is the inverse Boltzmann temperature and P is the probability distribution of dihedral angle, obtained from histograms constructed from the time series shown in the top and bottom panels.

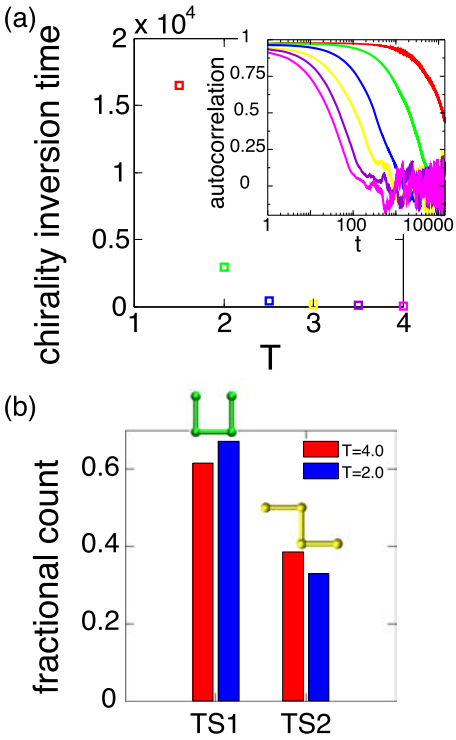

FIG. 4. Chiral inversion times and transition states of a single tetramer in a Lennard-Jones fluid at reduced density 0.66. (a) Characteristic relaxation time as a function of temperature. The inset shows the autocorrelation function of chirality over a range of temperatures, from T = 1.5 (top) to 4.0 (bottom), in increments of 0.5. (b) Resolved frequency of occurrence for the transition states of a single tetramer in a mono-atomic liquid solvent as a function of temperature. The transition states are identified as tetramer configurations with a dihedral angle between $\phi_{ts}-\Delta\phi$ and $\phi_{ts}+\Delta\phi$, where $\Delta\phi$ is chosen to be 22.5°.

To understand further the inversion kinetics, we examined the characteristic time scale as well as the kinetic pathway for chiral inversion. In analyzing the characteristic time scale for inversion, we calculated a chirality autocorrelation function C_ζ for the solvated tetramer,

$$C_\zeta(\Delta t) = \frac{\langle \zeta(t)\,\zeta(t+\Delta t)\rangle}{\langle \zeta^2(t)\rangle} \tag{7}$$

at different temperatures. Next, we determined the time scale for inversion as the time constant from an exponential decay fit to the chirality autocorrelation function. Figure 4(a) and its inset show the temperature dependence of the characteristic time scales for chiral inversion and a representative behavior of the autocorrelation function, respectively. Clearly, we observe a strong temperature dependence of the time scale for chirality inversion.

To elucidate the kinetic pathway for chiral inversion, we identified the relative occurrence of traversal of the achiral ("*cis*" and "*trans*") transition states during inversion. Because the chirality measure ζ is exactly zero at the transition states, the chirality autocorrelation function C_ζ does not distinguish between the two geometrically distinct transition states. However, as shown in Fig. 2, a suitable definition of the dihedral angle allows us to distinguish between the transition states. Using the dihedral angle, we created histograms to determine the relative occurrence of each transition state as shown in Fig. 4(b). From the histograms, we observe that the solvated "*cis*" (or incomplete-square) configuration is more "stable" than the solvated "*trans*" (or crank-shaft) configuration. This observation is consistent with the free energy profile shown in Fig. 3, where the barrier height at the "*cis*" configuration (dihedral angle 0°) is lower than that at the "*trans*" configuration (dihedral angle 180°). Note that the "*cis*" configuration is considerably more compact than the "*trans*" configuration, as shown in Fig. 2. Evidently, this geometric distinction between the two transition states produces a difference in the solvation free energy and steric hindrance for the rates of crossing the respective transition barriers.

B. Liquid phase behavior

We now turn attention to the liquid-phase behavior of the tetramer model in the absence of solvent. In this study, we have considered a special case with the chirality renormalization parameter $\lambda = +0.5$. This parameter choice energetically favors local homochiral interactions. In analyzing the phase behavior, we utilized a traditional order parameter which characterizes the extent of chiral symmetry-breaking in the system. The enantiomeric excess (ee) provides a measure of chiral symmetry-breaking and is defined as[26,40]

$$\begin{aligned} ee &= \frac{n_L - n_D}{n_L + n_D}, \\ n_{L,D} &= \frac{N}{2} \mp \frac{1}{2}\sum_{i=1}^{N} \operatorname{sgn}\zeta_i, \end{aligned} \tag{8}$$

where n_L (corresponding to $-$ in the $\mp$ notation) and n_D (corresponding to $+$ in the $\mp$ notation) represent the number of left and right-handed molecules, respectively. In the context of our tetramer model, the chirality measure ζ also allows for the definition of a convenient symmetry-breaking order parameter. This alternative parameter is the average chirality, $\bar{\zeta} \equiv \frac{1}{N}\sum_{i=1}^{N}\zeta_i$, where N is the total number of tetramer molecules in the system. Note that the average chirality, unlike the enantiomeric excess in Eq. (8), assigns appropriately diminished weights to molecules near a transition state. Nevertheless, in most of our calculations, the enantiomeric excess is roughly equal to the average chirality.

First, we analyzed the time-dependent behavior of the average chirality of the system, starting from an enantiopure initial configuration. Here, and in the following, our system comprises of 1024 tetramer molecules. Figure 5 shows the time evolution of $\bar{\zeta}$ under isochoric conditions (tetramer number density 0.17) at two distinct temperatures ($T = 4.0$ and $T = 2.0$). At the higher temperature, the system tends rapidly towards a racemic condition with a vanishing average chirality as shown in Fig. 5(a). This behavior indicates that at this temperature, the entropic contributions (which favor racemic configurations) dominate over energetic contributions (which favor enantiopure configurations for the positive chiral bias) to the overall Helmholtz free energy. Therefore, at this high temperature, the system minimizes its free energy by adopting a racemic average chirality. At lower temperatures, it is expected that energetic contributions will dominate over entropy and thus favor enantiopure configurations. As shown

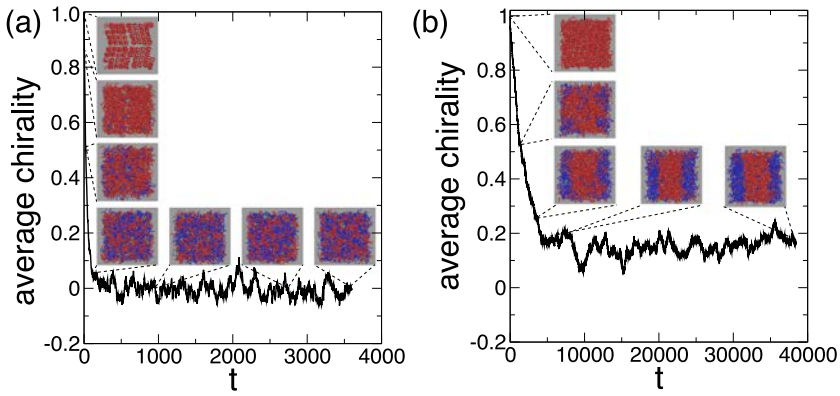

FIG. 5. Racemization behavior of a melt of chiral tetramer molecules initialized at an enantiopure configuration and reduced tetramer number density, 0.17 at temperatures (a) T = 4.0 and (b) T = 2.0. Here and in the following figures, the $\zeta > 0.33$ tetramers are drawn in red, and those with $\zeta < -0.33$ are drawn in blue.

in Fig. 5(b), we find that at $T = 2.0$, the system tends from enantiopurity towards a spatial symmetry-broken state with a low average chirality. In a system in which the enantiomeric excess is fixed, the phase behavior depicted in Fig. 11 (to be discussed in Sec. III C) would apply, and the coexistence between two phases, one L-rich and the other D-rich, is indeed the expected equilibrium state at low enough temperatures. In the cases considered in our work, however, the number of tetramers, volume (or pressure), and temperature, but not the enantiomeric excess, are held fixed. Under these conditions, it is always thermodynamically favorable for one of the two coexisting phases to grow at the expense of the other. We anticipate that after a sufficiently long time, the positive free energy cost associated with the interface, and statistical fluctuations, will lead one chiral phase to grow at the expense of its mirror image phase.

Motivated by a recent experiment demonstrating the coexistence of immiscible isotropic chiral liquids,[57] we also examine additional aspects of chirality-induced phase separation in our model system. In contrast to our model with intrinsic chiral molecules, the experimental system consists of nominally achiral flexible organic molecules which tend to pack into chiral domains. Despite this apparent distinction, our approach should prove useful in demonstrating the phenomenology observed for the flexible molecules. For this purpose, we investigated the propensity for our system to phase separate into chiral domains using isochoric MD simulations over a wide range of temperatures. Consistent with the symmetry breaking result in Fig. 5(b), we find that our system also phase separates at temperatures below $T = 2.0$.

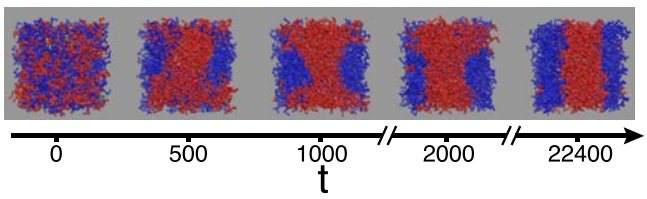

FIG. 6. Chirality-induced liquid-liquid phase separation. The time sequence of snapshots shows the evolution of a system of tetramer molecules at T = 1.4 and reduced tetramer number density, 0.17. The initial configuration is obtained from calculations at T = 4.0 and corresponds to a spatially homogenous racemic condition. In the snapshots, we indicate near achiral configurations with a green color. Such configurations correspond numerically to a chirality measure $|\zeta| < 0.33$.

Figure 6 shows a representative time sequence of snapshots of the system at $T = 1.4$. In the snapshots, the tetramers are color-coded according to their chirality. In the initial configuration ($t = 0$), the system is spatially homogenous with respect to chirality (i.e., racemic). A close inspection of the initial configuration also shows a few molecules in the neighborhood of a transition state, albeit short-lived. As time proceeds, the tetramers deform, switch chirality, and diffuse in such a way that local enantiopure configurations are favored. A natural consequence of this behavior is the emergence of a clear interface separating the immiscible chiral liquids as shown in the final snapshot in Fig. 6. It is worth emphasizing that the two liquids are expected to have identical thermodynamic and dynamic properties and to only differ by chirality. In addition, similar to the cited recent experiment,[57] the domains formed here contain isotropic liquids. That is, the liquids do not show significant nematic or other liquid-crystal order.

In terms of the enantiomeric excess, the overall system maintains a nearly racemic (vanishing *ee*) configuration throughout the entire calculation shown in Fig. 6. However, after phase separation, the two immiscible liquids individually are essentially enantiopure. To quantify the chirality of the immiscible phases, we calculated the local enantiomeric excess in distance slices normal to the emergent interface. Figure 7 shows the enantiomeric excess for a similar

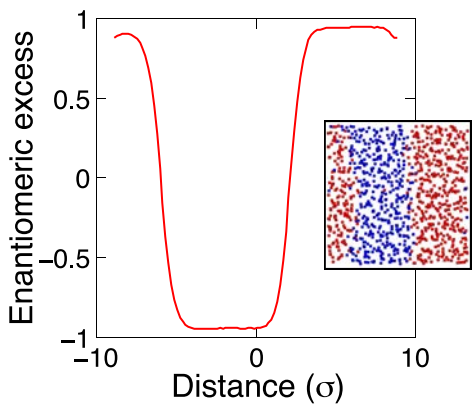

FIG. 7. Phase separation of two chiral liquids at T = 1.4 and reduced tetramer number density, 0.17. The main figure shows the local enantiomeric excess profile as a function of distance normal to the planar interface formed by the coexisting chiral liquids. The inset shows a representative snapshot of the center of masses of the tetramers color-coded by chirality.

calculation as in Fig. 6. The inset of Fig. 7 shows a corresponding snapshot of the system density distribution based on the tetramer centers of mass and colored by chirality. Both the inset and the main figure show that the immiscible phases have enantiomeric excesses that are essentially equal in magnitude but different in sign. In addition, it is shown that near the interface, the local enantiomeric excess is zero, and one would expect that, due to the strong repulsion between clusters of opposite chirality, a depletion in the local density would occur near this region. The density depletion is more evident on analysis of the inset in Fig. 7. Overall, our phase separation results are consistent with the phenomenology observed with organic flexible molecules.[57]

The appearance of coexisting opposite-chirality liquids illustrated in Figs. 6 and 7 evidently stems from disparate rates of diffusion in contrast to chiral inversion for the individual tetramers. Of course, the self-diffusion constant, as well as the inversion rate, is expected to be identical for each enantiomer. Starting at sufficiently low temperature in a homogenous racemic configuration, the relatively rapid diffusion in contrast to inversion allows tetramers of a given chirality to find one another, forming uniform chirality clusters that are not in jeopardy from frequent chiral inversions. These clusters grow and aggregate, finally forming system-spanning phases. The interfaces between the resulting neighboring phases involve a positive free energy (positive surface tension), which is minimized at least temporarily by adopting an essentially planar geometry between the contacting planar phase slabs. Of course the overall free energy would be lowered if one of the two coexisting liquids could "bully" the other one to reverse its chirality and thus lead to the system becoming a single interface-free isotropic liquid. However, there is no directed driving force present in the slab geometry of coexisting phases to prefer one outcome over its mirror image version. Consequently, it is expected to take a very long time for the low temperature system to experience a sufficiently disruptive fluctuation to banish the planar interfaces and end up with just one chiral liquid.[58,59] In this connection, it is worth reminding readers that the experimental microscopic observation of isotropic chiral liquids[57] involves essentially undetectable movement of the interfaces separating the coexisting phases.

The obvious molecular dynamics scenario to circumvent the coexistence situation at low temperature would employ an initial configuration that is enantiopure. Presuming that the chosen temperature was well below the symmetry-breaking critical point for the given density, one should observe essentially undisturbed persistence of the non-zero average chirality sign as time progresses.

Figure 8 shows three representative trajectories of many generated for the time evolution of the average chirality of the system. We find that as expected the system does not display any preference for a specific final handedness, i.e., positive and negative average chiralities appear to be equally likely. In addition, we find that a significant fraction of the runs persist in the near-racemic configurations for the entire course of our calculations. These observations reveal the highly stochastic nature of spontaneous chiral symmetry breaking below an upper consolute temperature.

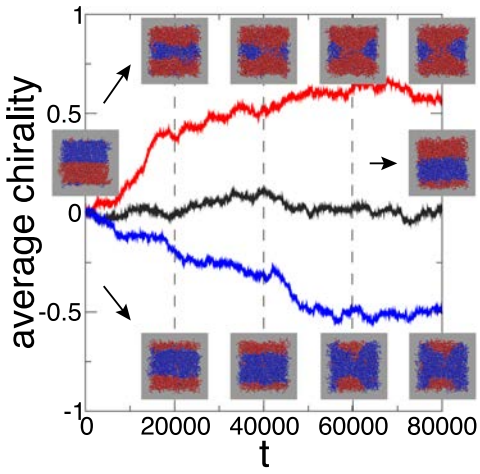

FIG. 8. Chiral symmetry breaking in the tetramer model at $T = 1.4$ and $p = 1$. This choice of pressure corresponds to an average reduced tetramer number density of 0.17. Three representative realizations and corresponding time-sequence of snapshots are shown. The realizations correspond to a D-dominant liquid (top), a racemic liquid (middle), and an L-dominant liquid (bottom). All isobaric MD calculations are initialized with exactly the same position configuration but differ in the assigned initial velocities, which are sampled from a Maxwell-Boltzmann distribution.

C. Chiral solid phase

Upon further cooling, a natural expectation is the formation of a crystalline phase. However, crystallization from a liquid phase via direct simulation is known to be often challenging for molecular systems, such as we consider here.[60,61] In our calculations, direct molecular dynamics attempts to crystallize our model system thus far have proved unsuccessful. Nevertheless, to gain insight into the possible crystal phases of our system, we first determined the ground state for a pair of tetramers for three specific choices of a chiral renormalization parameter, λ. In particular, we consider $\lambda = -0.5$, which energetically favors racemic interactions, $\lambda = 0$, which does not directly favor chiral interactions, and $\lambda = +0.5$, which strongly favors enantiopure interactions. In determining the ground state energies and configurations for tetramer pairs, we performed a series of isochoric MD simulations of a system of two tetramers, from which we sampled about 50 configurations for inherent structure calculations for each renormalization parameter. Finally, for each λ, we then determined the ground state as the minimum energy obtained from these calculations.

Figure 9 shows the results for the ground state energies and configurations for tetramer pairs at each value of the chirality renormalization parameter. Here again, the tetramers are colored according to their chirality. As expected, the ground state configurations for $\lambda = +0.5$ and $\lambda = -0.5$ are enantiopure and racemic pairs, respectively. Although both cases have the same magnitude of chiral renormalization, we find that the ground state energy for the enantiopure pair is slightly lower than that for the racemic pair. This suggests that the tetramer model without chiral renormalization at low to moderate pressure may intrinsically prefer enantiopure configurations. In fact, the solid phase for hydrogen peroxide, from which we draw inspiration for the tetramer model, is enantiopure.[47,48] However, in contrast to our tetramer model,

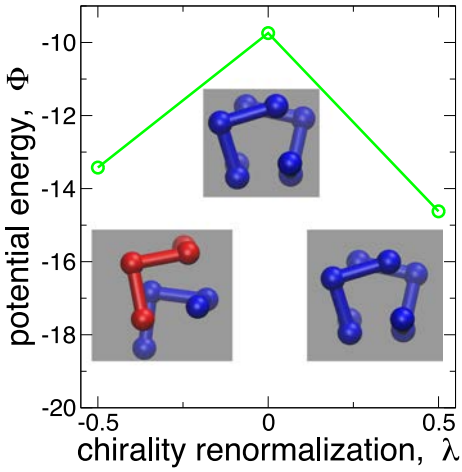

FIG. 9. Estimated ground state energies and configurations for a pair of tetramers as a function of a chirality renormalization parameter. The numerical values for the potential energy for $\lambda = -0.5$, 0.0, and +0.5 are −13.42, −9.74, and −14.62, respectively. Note that for these calculations, the potential energy cutoff is turned off.

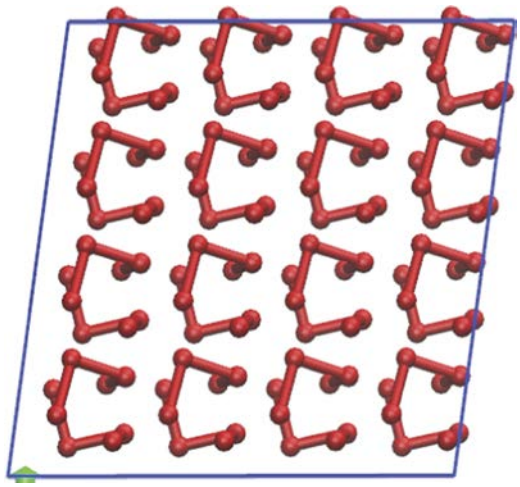

FIG. 10. Lowest energy structure of enantiopure crystal from isothermal-isobaric and inherent structure calculations for 128 tetramer molecules. Note the alignment of subsequent rows of tetramer molecules in the crystal.

hydrogen peroxide is clearly stabilized by hydrogen bonding. Incorporation of chiral renormalization may thus prove useful in coarse-graining the likely chiral effects of hydrogen bonding in a broader range of models.

Without chiral renormalization, i.e., $\lambda = 0$, the ground state energy is significantly higher than the corresponding energy of the renormalized cases, by a factor of approximately $1 + |\lambda|$, as shown in Fig. 9. We note that this result is by construction, as the chirality renormalization parameter increases the interparticle energy scale as shown in Eq. (4). The ground state configuration for $\lambda = 0$ case is found to be enantiopure. This result is consistent with the relative results of the ground state calculations for the homochiral ($\lambda = +0.5$) and heterochiral ($\lambda = -0.5$) renormalizations. A direct substitution of the ground state configurations for the homochiral- and heterochiral-bias cases into the renormalization-free potential energy function suggests that the enantiopure configuration should be ground state for $\lambda = 0$.

Our two-tetramer ground state calculations also suggest that careful tuning of the chiral renormalization parameter should in principle lead to the formation of either conglomerate (enantiopure) or racemic crystals at sufficiently low temperatures. To determine possible crystal structures for our tetramer model, we first explore the mechanical stability (via constrained energy minimization) of geometrically reasonable initial configurations. Next, we selected successful candidate crystal structures by visual inspection of the configurations. Using those successful configurations, we then performed a series of low temperature isobaric MD simulations at $p = 0.01$. Note that we allow the periodic box dimensions to fluctuate independently to enable the system find its preferred unit cell. We then examined the final structure to determine if it is indeed crystalline.

Using the approach outlined above for $\lambda = +0.5$, we consistently obtained a triclinic enantiopure structure as the final configuration. The snapshot of the inherent structure for this result is shown in Fig. 10. From visual inspection of Fig. 10, the structure appears to be a perfect crystal. This is evident by noting the apparent spatial alignment of the subsequent rows of the molecular crystals. Also note that each periodic unit for the crystal here consists of two tetramer molecules. That is, the unit cell of the crystal contains a basis of two chirally equivalent tetramers. Note that the tetramer pair is similar to the ground state configuration for $\lambda = +0.5$ in Fig. 9. The crystal structure shown in Fig. 10 has a reduced potential energy $\Phi = -29.4$ (on a per-tetramer basis) and a reduced number density $\rho = 0.24$.

This enantiopure crystal identification, in addition to the liquid-state behavior described in Section III B, leads to the qualitative pattern shown in Fig. 11 for the chiral symmetry breaking behavior when $\lambda = +0.5$, where the tetramer number density corresponds to low to moderate pressure. Above a critical temperature T_c, the liquid phase is racemic (ee = 0), indicated in Fig. 11 by a vertical line. As temperature declines through T_c, spontaneous chiral symmetry breaking takes over, producing bifurcation of the ee equilibrium so as to create

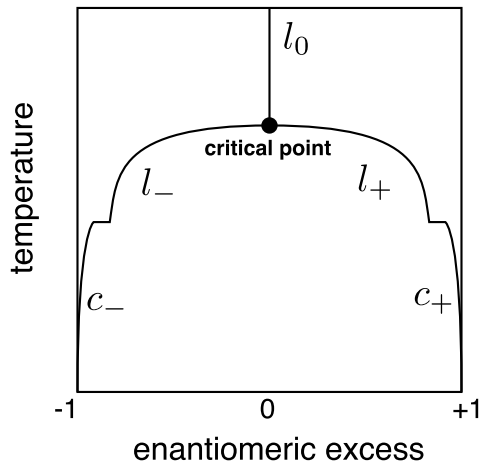

FIG. 11. Qualitative phase diagram for chiral symmetry breaking at low to moderate pressures for a positive chirality renormalization parameter. The labels l and c represent liquid and crystal phases, respectively. The subscripts 0, −, and + represent racemic, L-rich, and D-rich overall compositions, respectively.

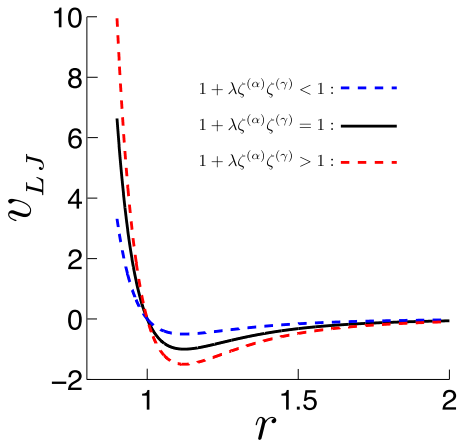

FIG. 12. Reversal of pair energy potential for a chirality renormalized Lennard-Jones function.

a critical point analogous to that involved in the familiar liquid-vapor phase behavior. Because the ee, or equivalently the $\langle\bar{\zeta}\rangle$, are scalar quantities, it is an important open question whether this critical behavior for chiral symmetry breaking exhibits the same leading-order critical exponents as the three-dimensional Ising model.[62] Concerning comparison with Ising model critical exponents, it will be important eventually to determine the response (susceptibility) of our tetramer model to the inclusion of an external field proportional to $\sum_{i=1}^{N}\zeta_i$.

A final basic point needs to be stressed regarding the behavior of the chirality energy renormalization assumption, as presented in Eq. (4) and Fig. 12. A non-zero choice for the renormalization strength parameter λ has the effect of lowering the minimum of the intramolecular L-J pair functions for like ($\lambda > 0$) or unlike ($\lambda < 0$) chirality neighbors. Under low to moderate pressure conditions, this dominates the configurational preferences for the condensed phases involved. But it is important to realize that a fundamental reversal must occur at sufficiently high external pressure. The reason is that neighboring monomer units are then squeezed into much closer contact, leaving the neighborhood of the L-J minima, and forced into the strongly repelling core region. Consequently, increasing the pressure on the $\lambda = 0.50$ enantiopure crystal just described must eventually cause it to be replaced by a thermodynamically more stable racemic crystal. The reverse situation would be true for the $\lambda = -0.5$ case. These pressure-induced chirality inversions, and their possible liquid phase analogs, provide a rich set of opportunities for future study.

IV. CONCLUSION

We have developed a three-dimensional off-lattice molecular model for studying aspects of many-body chirality phenomena. Our model system, inspired by the real four-atom substances hydrogen peroxide and hydrogen disulfide, consists of tetramer molecules with well-defined chirality as determined by their dihedral angles. Two key features distinguish our new model: (i) the molecules undergo chiral inversion as they interconvert between two enantiomeric forms and (ii) a direct control exists over local homochiral versus heterochiral tetramer interactions. Based on our calculations in this work, these two features are sufficient to prescribe a range of phenomena including chiral inversion kinetics, liquid-liquid chiral phase separation, and the existence of a conglomerate solid phase. Furthermore, our calculations suggest that the tetramer model may be useful in studying a variety of physical mechanisms relevant to chiral symmetry breaking, including the recently proposed eutectic tuning.[44]

Finally, we note that our tetramer model may be extended to include chemical reactions. In particular, it is possible to create a potential energy function that enables two achiral dumbbell reactants to combine chemically and form a chiral tetramer. The inclusion of this property should, in principle, generalize the tetramer model to describe both chemical and physical mechanisms for chiral symmetry breaking.

[1]A. Guijarro and M. Yus, *The Origin of Chirality in the Molecules of Life* (RSC, Cambridge, 2009).
[2]W. Lough and I. Wainer, *Chirality in Natural and Applied Science* (Blackwell, Oxford, 2002).
[3]L. A. Nguyen, H. He, and C. Pham-Huy, Int. J. Biomed. Sci. **2**, 85 (2006).
[4]I. Agranat, H. Caner, and J. Caldwell, Nat. Rev. Drug Discovery **1**, 753 (2002).
[5]R. Noyori, *Asymmetric Catalysis in Organic Synthesis* (Wiley, NY, 1994).
[6]C.-D. Wu, A. Hu, L. Zhang, and W. Lin, J. Am. Chem. Soc. **127**, 8940 (2005).
[7]A. Stalcup, Annu. Rev. Anal. Chem. **3**, 341 (2010).
[8]J. B. Pendry, Science **306**, 1353 (2004).
[9]P. F. Damasceno, A. S. Karas, B. A. Schultz, M. Engel, and S. C. Glotzer, Phys. Rev. Lett. **115**, 158303 (2015).
[10]C. Tschierske, Angew. Chem. Int. Ed. **52**, 8828 (2013).
[11]H. H. Wensink and G. Jackson, J. Chem. Phys. **130**, 234911 (2009).
[12]S. F. Swallen, K. L. Kearns, M. K. Mapes, Y. S. Kim, R. J. McMahon, M. D. Ediger, T. Wu, L. Yu, and S. Satija, Science **315**, 353 (2007).
[13]K. Adrjanowicz, K. Kaminski, M. Paluch, K. L. Ngai, and L. Yu, J. Chem. Phys. **136**, 234509 (2012).
[14]K. Adrjanowicz, K. Kaminski, M. Paluch, and K. Niss, Cryst. Growth Des. **15**, 3257 (2015).
[15]K. Adrjanowicz, K. Kaminski, Z. Wojnarowska, M. Dulski, L. Hawelek, S. Pawlus, M. Paluch, and W. Sawicki, J. Phys. Chem. B **114**, 6579 (2010).
[16]R. Breslow, Tetrahedron Lett. **52**, 2028 (2011).
[17]S. F. Mason and G. E. Tranter, Proc. R. Soc. London, Ser. A **397**, 45 (1985).
[18]J. Bada, Nature **374**, 594 (1995).
[19]D. K. Kondepudi and G. W. Nelson, Nature **314**, 438 (1985).
[20]G. Lente, Phys. Chem. Chem. Phys. **9**, 6134 (2007).
[21]F. Frank, Biochim. Biophys. Acta **11**, 459 (1953).
[22]T. Shibata, H. Morioka, T. Hayase, K. Choji, and K. Soai, J. Am. Chem. Soc. **118**, 471 (1996).
[23]K. Soai, T. Shibata, H. Morioka, and K. Choji, Nature **378**, 767 (1995).
[24]D. G. Blackmond, C. R. McMillan, S. Ramdeehul, A. Schorm, and J. M. Brown, J. Am. Chem. Soc. **123**, 10103 (2001).
[25]H. W. Hatch, F. H. Stillinger, and P. G. Debenedetti, J. Chem. Phys. **133**, 224502 (2010).
[26]F. Ricci, F. H. Stillinger, and P. G. Debenedetti, J. Phys. Chem. B **117**, 602 (2013).
[27]F. Jafarpour, T. Biancalani, and N. Goldenfeld, Phys. Rev. Lett. **115**, 158101 (2015).
[28]H. C. Ottinger, *Stochastic Processes in Polymeric Fluids* (Springer Verlag, Berlin, 1996).
[29]F. Latinwo and C. M. Schroeder, Macromolecules **46**, 8345 (2013).
[30]H. Kuhn, Angew. Chem. Int. Ed. **11**, 798 (1972).
[31]H. Kuhn, Curr. Opin. Colloid Interface Sci. **13**, 3 (2008).
[32]M. Bolli, R. Micura, and A. Eschenmoser, Chem. Biol. **4**, 309 (1997).
[33]M. M. Green and B. A. Garetz, Tetrahedron Lett. **25**, 2831 (1984).
[34]G. F. Joyce, G. M. Visser, C. A. A. van Boeckel, J. H. van Boom, L. E. Orgel, and J. van Westrenen, Nature **310**, 602 (1984).
[35]P. Sandars, Origins Life Evol. Biospheres **33**, 575 (2003).
[36]C. Blanco and D. Hochberg, Phys. Chem. Chem. Phys. **13**, 839 (2011).
[37]J. T. Sczepanski and G. F. Joyce, Nature **515**, 440 (2014).
[38]D. G. Blackmond and M. Klussmann, Chem. Commun. **39**, 3990 (2007).

[39]C. Viedma, Astrobiology **7**, 312 (2007).
[40]D. G. Blackmond, Cold Spring Harbor Perspect. Biol. **2**, a002147 (2010).
[41]C. Viedma, Phys. Rev. Lett. **94**, 065504 (2005).
[42]D. K. Kondepudi, R. J. Kaufman, and N. Singh, Science **250**, 975 (1990).
[43]C. Viedma, J. E. Ortiz, T. de Torres, T. Izumi, and D. G. Blackmond, J. Am. Chem. Soc. **130**, 15274 (2008).
[44]W. L. Noorduin, T. Izumi, A. Millemaggi, M. Leeman, H. Meekes, W. J. P. V. Enckevort, R. M. Kellogg, B. Kaptein, E. Vlieg, and D. G. Blackmond, J. Am. Chem. Soc. **130**, 1158 (2008).
[45]T. G. Lombardo, F. H. Stillinger, and P. G. Debenedetti, Proc. Natl. Acad. Sci. U. S. A. **106**, 15131 (2009).
[46]R. Ball and J. Brindley, Origins Life Evol. Biospheres **46**, 81 (2016).
[47]S. C. Abrahams, R. L. Collin, and W. N. Lipscomb, Acta Crystallogr. **4**, 15 (1951).
[48]W. R. Busing and H. A. Levy, J. Chem. Phys. **42**, 3054 (1965).
[49]H. H. Wensink and G. Jackson, J. Phys.: Condens. Matter **23**, 194107 (2011).
[50]S. Varga and G. Jackson, Chem. Phys. Lett. **377**, 6 (2003).
[51]R. I. Cukier and S. A. Seibold, J. Phys. Chem. B **106**, 12031 (2002).
[52]R. L. Redington, W. B. Olson, and P. C. Cross, J. Chem. Phys. **36**, 1311 (1962).
[53]R. H. Hunt, R. A. Leacock, C. W. Peters, and K. T. Hecht, J. Chem. Phys. **42**, 1931 (1965).
[54]S. Plimpton, J. Comput. Phys. **117**, 1 (1995).
[55]F. H. Stillinger and T. A. Weber, Science **225**, 983 (1984).
[56]F. H. Stillinger and T. A. Weber, Phys. Rev. A **28**, 2408 (1983).
[57]C. Dressel, T. Reppe, M. Prehm, M. Brautzsch, and C. Tschierske, Nat. Chem. **6**, 971 (2014).
[58]S. Toxvaerd, Phys. Rev. Lett. **85**, 4747 (2000).
[59]S. Toxvaerd, Int. J. Mol. Sci. **10**, 1290 (2009).
[60]R. Martoňák, A. Laio, and M. Parrinello, Phys. Rev. Lett. **90**, 075503 (2003).
[61]M. Salvalaglio, T. Vetter, M. Mazzotti, and M. Parrinello, Angew. Chem. Int. Ed. **52**, 13369 (2013).
[62]H. E. Stanley, *Introduction to Phase Transitions and Critical Phenomena* (Oxford University Press, USA, 1987).